

Subgrid scale formulation of optical flow for the study of turbulent flow

C. Cassisa · S. Simoens · V. Prinet · L. Shao

Received: date / Accepted: date

Abstract We propose a new formulation of optical flow in the case of passive scalar or solid particles spreading in turbulent flows. The flow equation is defined from the scalar transport equation and a decomposition of our physical quantities (velocity and concentration fields) into two contributions, large and small scales, to account for the lack of spatial resolution in processed images. A subgrid scale model is introduced to model the small scale contribution. Comparisons are made with existing optical flow methods and Particle Image Velocimetry (PIV) on synthetic and real sequences. The improvement of the estimation of velocity field by the proposed formulation is discussed in the case of a scalar turbulent propagation.

Keywords Motion Estimation · Differential Optical Flow · Turbulence · Large Eddy Decomposition · Subgrid Model

1 Introduction

The study of fluid flow is one of the main challenge in application domains such as aeronautic, acoustic, or environmental sciences. Conclusions drawn from the analysis of experiments are strongly linked to the methodology used for motion estimation.

Particle Image Velocimetry (PIV) technique (Adrian [1]) is most commonly used in laboratories to compute the velocity field of fluids from image sequences. It requires a

good synchronization between the successive acquisitions of images of particles seeding a flow. A laser pulse illuminate the fluid with a sheet of light. The particle images are then recorded at two consecutive instants on a CCD camera. This allows to freeze the particles seeding the fluid at two successive times of their displacements. The particles velocity field can then be estimated from the resulting image sequence (pairs of images or long temporal sequence).

PIV technique is attractive for its simplicity. The motion field is retrieved by searching the local displacement that maximizes the cross-correlation between two interrogation windows placed in each of the two images. This approach has proved to be very efficient when satisfying various criteria related to the density of particles or to the local gradient of the studied flow. Nevertheless, there are several limiting factors. At first, the size of the window needs to be chosen carefully: if too small, the cross-correlation peak might not be reliable ; if too big, the particles in the windows might be animated by different movements due to local inhomogeneities of the flow; because PIV method estimates a single velocity vector representing the majority displacement of particles in the window, the resulting velocity field will be over-smoothed. In these two cases, the estimated velocity field might be either noisy, either too smooth, or even incorrect. In addition, PIV approach cannot be used for scalar field sequences, due to the absence of clear correlation peak in this type of images.

Optical Flow-based approaches have for advantage to provide a dense estimation of the flow velocity field. Nevertheless Optical Flow (OF) is less popular than PIV in fluid mechanic community because it is more sensitive to experimental noise and imaging conditions. An other reason is the seeding of the studied flows. OF methods are not usable where there is no seeding whereas PIV can be used as soon as there is a background homogeneous seeding. Nevertheless OF is particularly efficient to estimate a dense velocity

C. Cassisa* · S. Simoens · L. Shao
LMFA, CNRS UMR 5509, Ecole Centrale de Lyon, Ecully, France.
E-mail: {cyril.cassisa,serge.simoens,liang.shao}@ec-lyon.fr
* Now at Lab. of Turbulence, Tsinghua University, Beijing

V. Prinet
National Lab. of Pattern Recognition, Institute of Automation, Chinese Academy of Sciences, Beijing, China
E-mail: vprinet@gmail.com

field from scalar images acquired at successive instants (*e.g.* smokes propagation or clouds in meteorological images).

Optical Flow, as defined by Horn & Shunk [25] in the early 80's, is based on an *assumption of brightness conservation* over a small time interval : the grey-level I of a given object does not change locally between two image acquisitions at t and $t + \delta t$: $I(\mathbf{s}, t) = I(\mathbf{s} + \delta \mathbf{d}, t + \delta t)$, with \mathbf{s} the coordinates of the object at time t and $\delta \mathbf{d}$ its shift between the two acquisitions. A first order Taylor development leads to the differential form of the OF equation:

$$\frac{\partial I(\mathbf{s}, t)}{\partial t} + \mathbf{v} \cdot \nabla I(\mathbf{s}, t) = 0 \quad (1)$$

where $\mathbf{v} = \frac{\delta \mathbf{d}}{\delta t}$ is the apparent velocity of the object and ∇ represents the spatial gradient. This basic equation establishes the relationship between the observed data/image I and the displacement vector $\delta \mathbf{d}$ to estimate. However, because the motion is computed in a two or three dimensional space, equation (1) is under-constrained and a regularization term needs to be added in order to satisfy the unicity of the solution. This regularization term takes commonly the form of a 'smoothing factor', which put spatial and/or temporal constraints on \mathbf{v} .

The brightness consistency hypothesis, on which most OF-based approaches lie, is well suited for the estimation of rigid motions. However, insofar we are concerned with fluid motion, it is not a valid assumption any more. In an attempt to model the physical behaviour of fluid flow, alternative formulations have been proposed : volume conservation (Amini [2], Bereziat et al. [8]), continuity equation (Corpetti et al. [17]), and generalized transport equation applied to particle images (Liu and Shen[29], Heitz et al. [22]). Besides, efforts have been put to improve the regularization term: some authors enforce divergence and vorticity constraints (Suter [46], Corpetti et al. [17]) or integrate Navier-Stokes equation (Ruhnau and Schnorr [35], Heitz et al. [22]). In particular in [22], Heitz et al. combine correlation and OF methods: they use the robustness (w.r.t. to noise and large displacements) of correlation technique to first estimate a coarse field, then to constrain the OF estimation. The idea is interesting but fails when applied to scalar quantities, because gradients become small and correlation peaks hardly detectable. A review paper Heitz et al. [23] (2010) reports and compare different solutions devised for fluid motion analysis and measurement.

The problem of turbulence is generally ignored in the flow equation of existing methods. However, in the reality most of the fluid flows around us are highly turbulent: atmospheric motions, ocean currents, vascular flows... Level of turbulence of the flow is controlled by the Reynolds number $Re = UL/\nu$ where U , L are the velocity and length scales of the flow and ν the kinetic viscosity of the fluid. For high Re , the flow is turbulent. The ratio between scale of large

eddy and smallest wave length of movements that can appear in the fluid (Kolmogorov scale [26]) is proportional to $Re^{3/4}$. This implies, that to get all scales which appear in the turbulent flow, time and space resolution have to be equivalent to $Re^{3/4}$ (for example, for atmospheric flows $Re \approx 10^{10}$). Generally, time and space image resolution are much sparser than the smallest scales. Depending to the rate of turbulence, missing information in the image sequence may not be neglected. The influence of these small scales cannot be computed but should be modeled.

In this work, we analyse turbulent fluid flows from image sequences, by linking the concentration of particles to the observed intensity in images. We propose a *Large Eddy Simulation (LES) decomposition* (Le Ribault et al. [34]) of the *transport equation* (Su and Dahm [44, 45]), where the influence of small scales is incorporated via a subgrid scale turbulent viscosity term. We add a spatial regularization function for unicity of the solution. The proposed mathematical formulation is a new approach for optical flow estimation. The estimated velocity field take into account effect of small scales through the turbulent viscosity.

Experimental results are illustrated on a synthetic sequence generated by Direct Numerical Simulation (DNS) (Carlier and Heitz [11]) and a fluid flow image sequence from laboratory experiment (Simoens et al. [38, 39]). We compare and validate our approach against correlation technique (Davis Lavisson software [28]) and a state-of-the-art algorithm (Corpetti et al. [17]).

The rest of the paper is organized as follows. In section 2, we first present our sub-grid transport equation model (TE-SGS) and formulate the problem of velocity field estimation from images as a maximum a posteriori estimation ; to retrieve the optimal solution, we propose a new efficient algorithmic based on a multigrid multi-resolution scheme. In section 3, we describe the experimental data and validation cases. We compare the results obtained from different approaches and discuss the advantages of our TE-SGS model in section 4. We conclude in section 5.

2 Methodology

This section describes our motion equation for the estimation of turbulent flows. The transport equation is filtered and small scale terms are modeled by a turbulent diffusion. The problem is formulated by a maximum a posteriori estimation. Solution is obtained by direct descent energy using an hybrid multiresolution technique.

2.1 Scalar transport equation (TE)

The velocity field of a passive scalar concentration C of a speck spreaded in a fluid is described by the scalar transport

equation (TE). In dimensionless form, it writes as follows (Batchelor [7]):

$$\frac{\partial C}{\partial t} + \nabla \cdot (C\mathbf{v}) - \frac{1}{Re Sc} \Delta C = 0 \quad (2)$$

where \mathbf{v} is the velocity of the concentration field. Time and space partial derivatives are noticed $\frac{\partial}{\partial t}$ and ∇ respectively; Δ is the Laplacian operator. Re and Sc are the Reynolds and Schmidt numbers.

If we assume that the fluid is incompressible, *i.e.* $\nabla \cdot \mathbf{v} = 0$, then equation (2) becomes :

$$\frac{\partial C}{\partial t} + \mathbf{v} \cdot \nabla C - \frac{1}{Re Sc} \Delta C = 0 \quad (3)$$

To account for the lack of 3D information contained in images, we make the coarse hypothesis that the fluid is in a two-dimensional (2D) turbulence, where the transport equation is considered only on the plane (x, y) . Hence, the motion analysis is entirely performed in the 2D space. The velocity component along the z -axis is considered null, *i.e.* $\mathbf{v} = (u, v)$, and first and second order spatial derivative operators writes $\nabla = \left(\frac{\partial}{\partial x}, \frac{\partial}{\partial y} \right)$ and $\Delta = \frac{\partial^2}{\partial x^2} + \frac{\partial^2}{\partial y^2}$ respectively. It is note worthy that it is possible to link a real 3D transport equation to a 2D apparent motion in the image (Liu and Shen [29]), thought we do not address this issue in the present work.

The concentration C of a scalar quantity (dust particles, humidity, ...) can be related to the image pixel intensity value I . For cloud motion analysis, some authors established empirically the following relation: $I \propto \int C dz$ (Corpetti et al. [17]) or $I \propto (\int C dz)^{-1}$ (Zhou et al. [51]), where z is the observation depth. More recently an more physical relationship was established for cloud motion in Heas et al. [24].

It is clear that depending on the substance carried by the flow studied this relationship must be modified In this paper, we consider a simpler case, and assume that the pixel grey-level value is directly proportional to the concentration C :

$$I(s, t) \propto \alpha C(s, t) \quad (4)$$

where α is a constant independent of time and space. In other words, we consider that $\delta z / \delta x \ll 1$, $\delta z / \delta y \ll 1$.

We can notice that for case with apparent diffusion (solid particle) of the transported quantity ($Sc \gg 1$), equation (3) becomes equivalent to the differential OF equation as proposed by Horn and Schunck [25] (c.f. equ. 1).

2.2 Filtered transport equation with a subgrid scale model (TE-SGS)

Scalar transport equation defines the evolution of passive scalar concentration C as a function of velocity \mathbf{v} . Thus, knowing the passive scalar concentration at two successive instants in a plane of interest, we could simply retrieve the

velocity field by solving the TE (equation 3). However, in images acquired under controlled conditions during laboratory experiments or in satellite images for the study of atmospheric phenomena, we are limited by spatial and time resolutions: acquisition period δt and pixel size $\delta = (\delta x, \delta y)$ are both fixed. In most cases (especially for $Re \gg 1$), they are too large compared to the characteristic scales of turbulence itself. Nevertheless small scales displacements are important because they strongly influence the observed large scale motion of the studied concentration field (Cui et al. [18]). In this sub-section, we derive a new fluid motion equation, by integrating sub-pixels (*i.e.* non-observed) effects into the scalar transport equation.

Let us write C^+ the observed scalar concentration related to large scales. C^+ is the filtered value of the instantaneous scalar C over the pixel size δ . Formally, it results from the convolution of C with a filter $G()$ in 2D :

$$C^+(\mathbf{s}) = \int_{\delta} C(\mathbf{s} - \mathbf{r}) G(\mathbf{r}) d\mathbf{r} \quad (5)$$

where $\mathbf{s} = (x, y)$ is a pixel, $\mathbf{r} = (r_x, r_y)$ is the characteristic length of the filter in the x and y directions, δ the integration surface. The filter $G(\mathbf{r})$ can be defined as:

$$G(\mathbf{r}) = \begin{cases} 1/\delta & \text{if } |\mathbf{r}| < \delta/2 \\ 0 & \text{elsewhere} \end{cases} \quad (6)$$

Now, filtering the scalar transport equation (equ. 2) by $G()$, and taking advantage of the linearity of the filter, we obtain :

$$\frac{\partial C^+}{\partial t} + \nabla \cdot (C\mathbf{v})^+ - \frac{1}{Re Sc} \Delta C^+ = 0 \quad (7)$$

In addition, similarly to Large Eddy Simulation (LES) (Le Ribault et al. [34]), we consider that the instantaneous passive scalar concentration field verifies: $C = C^+ + C^-$, where C^- represents the small scale contribution. Accordingly, we propose to re-write $(C\mathbf{v})^+$:

$$(C\mathbf{v})^+ = C^+ \mathbf{v}^+ + \tau \quad (8)$$

where τ is the residual stress tensor: $\tau = L + R + CS$ and $L = (C^+ \mathbf{v}^+)^+ - C^+ \mathbf{v}^+$ is the Leonard stress, $R = (C^- \mathbf{v}^-)^+$ is the subgrid Reynolds stress, and $CS = (C^+ \mathbf{v}^-)^+ - (C^- \mathbf{v}^+)^+$ is the Cross-stress. Hence, the filtered TE becomes :

$$\frac{\partial C^+}{\partial t} + \nabla \cdot (C^+ \mathbf{v}^+) + \nabla \cdot \tau - \frac{1}{Re Sc} \Delta C^+ = 0 \quad (9)$$

For incompressible fluid, equation (9) can be simplified and expresses as :

$$\frac{\partial C^+}{\partial t} + \mathbf{v}^+ \cdot \nabla C^+ + \nabla \cdot \tau - \frac{1}{Re Sc} \Delta C^+ = 0 \quad (10)$$

To define τ , we borrow the concept of turbulent viscosity :

$$\tau = -D_t \nabla C^+ \quad (11)$$

with D_t a turbulent diffusion coefficient ; we define it as a statistical constant over the space domain.

Finally, inserting equation (11) into (10) leads to:

$$\frac{\partial C^+}{\partial t} + \mathbf{v}^+ \cdot \nabla C^+ - \left(\frac{1}{Re Sc} + D_t \right) \Delta C^+ = 0 \quad (12)$$

Such subgrid scalar transport equation (TE-SGS) is a new approach for OF estimation. At the best of our knowledge nobody took into account for subgrid scale effect of the small turbulent scale on flow motion estimation with OF formulation. Note that for high Reynolds number ($Re \gg 1$) or scalar with low molecular diffusion ($Sc \gg 1$), the contribution from turbulent diffusion becomes large compared to molecular diffusion ; it is the case, for example, for dust cloud particles in the atmosphere. Some works as Nomura et al. [30], Haussecker and fleet [21] or Garbe and al. [20] add a diffusion term with space and time variability but they accounted for physical effect under molecular or thermal similarity concept. 2) The problem of variability of D_t is classic in turbulent subgrid scale theory modelling discussions. It is known ([36,37]) that even in case of the strong inhomogeneous turbulent flow, for such proposed diffusion modelling at subgrid scale level, if this scale is small compared to the largest turbulent scales (that is the case most of time). The diffusion coefficient D_t can be approximated by a constant, except near the wall in wall bounded turbulent flow which is not the present case. This significates non variability neither in time and space. The main part of spectral subgrid scale modelling (Chollet and Lesieur [15]) demonstrates the validity of such hypothesis. Nevertheless to discuss such hypothesis is beyond the scope of this paper. The last point concern with establishing the constant diffusion coefficient via the formula of Deardorff [19]:

$$q_{sgm} = C_{sgm} * \left(\frac{D_t}{\Delta} \right)^2 \quad (13)$$

where Δ is the filter size (mesh size), q_{sgm} is the turbulent subgrid scale kinetic energy. Generally it is unknown but can be approximated by the knowledge of the power spectrum E_{uu} that is given or deductible from experimental fact or theory even for real atmosphere. In the present case, E_{uu} is estimated with a simple theoretical model using power law assumption from K_c to ∞ for E_{uu} (Comte-Bellot and Corsin [16]). This gives :

$$q_{sgm} = \frac{3}{2} * \int_{K_c}^{\infty} E_{uu}(K) dK \quad (14)$$

where $K_c = \frac{\pi}{\Delta}$. The constant C_{sgm} usually takes values around 0.1 (Deardorff [19]). This is what we have done for the two below tests.

From equations (13) and (14) we obtain :

$$D_t = \Delta * \left(\frac{3}{2 C_{sgm}} \int_{K_c}^{\infty} E_{uu}(K) dK \right)^{\frac{1}{2}} \quad (15)$$

Our modelling, to account for subgrid scale turbulence in the estimation of the local velocity field, is thus perfectly determined knowing the power spectrum and the filter size.

2.3 Motion field estimation

2.3.1 Introduction

Equation (12) defines the subgrid transport equation of the scalar C^+ . It establishes the relationship between the observed quantity C^+ and the unknown velocity vector \mathbf{v}^+ , at each point \mathbf{s} of the image domain. However, the resolution of equation (12) is not possible (it is a mathematically ill-posed equation), unless a regularization term is added.

At this point, one should make two remarks. The first one concerns the nature of the observed variable C^+ and of the unknown \mathbf{v}^+ . Fluid mechanics would consider equation (12) as a pure deterministic model. However, the observation C is known with a certain degree of uncertainty, due in particular to the stochastic process of imaging conditions. Consequently, the estimated velocity field, itself, can be estimated only up to a certain accuracy.

As for the second remark, one can notice that equation (12) describes the evolution of each point, or particle, independently, in the fluid. It is reasonable however to assume that nearby points are not totally independent, but are animated by similar motions. Hence, contextual constraints ought to be added to the model.

The two comments above motivated us to formulate the problem of motion estimation, as defined primarily by equation (12), in a probabilistic framework. More precisely, Markov Random Fields (MRF) theory provides us with the theoretical foundations necessary to deal with the issues of i) modelling the uncertainty , ii) modelling interdependencies between neighbor variables. A recall on MRF is not the scope of this article, we refer to Stan [43] or Winkler [50] for interested readers. In the rest of the section, for the sake of simplicity, we will use the notation \mathbf{v} instead of \mathbf{v}^+ , and C , instead of C^+ .

We treat \mathbf{v} and C as two random variables, the unknown and the observation respectively, defined at each point \mathbf{s} of the domain. $C(\mathbf{s})$ takes values in \mathbf{R}^+ , while $\mathbf{v}(\mathbf{s})$ is a continuous $2D$ variable bounded by $\Gamma =]\mathbf{v}_{\min}, \mathbf{v}_{\max}[$. Hence, $\mathbf{v} = \{\mathbf{v}(\mathbf{s}) \mid \forall \mathbf{s} \in \Omega\}$ describes the velocity field on the entire image domain Ω , with $card(\Omega) = N$. similarly, we coin $C = \{C(\mathbf{s}) \mid \forall \mathbf{s} \in \Omega\}$. Using Hamersley-Clifford theorem (Stan [43]), we define the probability to retrieve \mathbf{v} , given the

observation C , as follows:

$$P(\mathbf{v}|C) = \frac{1}{Z} \exp\{-E(\mathbf{v}, C)\} \quad (16)$$

$$E(\mathbf{v}, C) = \sum_{k \in K} V_k(\mathbf{v}, C) \quad (17)$$

Z is the normalization factor known as the partition constant. K is the set of all cliques. $E(\cdot)$ is the so-called Gibbs energy and V_k the associated potential functions.

Hence, we seek for the best solution $\hat{\mathbf{v}}$ that maximizes the posterior probability $P(\mathbf{v}|C)$, or equivalently, that minimizes the energy $E(\mathbf{v}, C)$:

$$\hat{\mathbf{v}} = \arg \min_{\mathbf{v} \in \Gamma^N} E(\mathbf{v}, C) \quad (18)$$

The choice of an MRF framework, associated to efficient optimisation technique on graphs, enables to define the functional $E(\cdot)$ with a certain flexibility (Szeliski and al. [47], Kolmogorov and Zabih [27]). Alternative methods to solve energy minimisation problems defined similarly to (18), such as variational approaches (Horn and Schunk [25], Heitz and al. [23]), are efficient in practice only if $E(\cdot)$ is a convex function of the unknown \mathbf{v} . In the following, we detail the formulation of $E(\cdot)$ and the optimization procedure.

2.3.2 Energy model

In a classical way, we define single-site clique $S = \{\mathbf{s} \in \Omega\}$, and pairwise cliques $S2 = \{\mathbf{s}, \mathbf{t} \in \Omega^2 | \mathbf{t} \in \mathcal{N}_s\}$, such that $K = \{S, S2\}$. \mathcal{N}_s defines here a 4-pixels neighbor around \mathbf{s} .

Thus we rewrite more specifically the right hand side of equation (17):

$$\sum_{\mathbf{s} \in S} V_d(\mathbf{v}(\mathbf{s}), C(\mathbf{s})) + \alpha_p \sum_{(\mathbf{s}, \mathbf{t}) \in S2} V_p(\mathbf{v}(\mathbf{s}), \mathbf{v}(\mathbf{t})) \quad (19)$$

The weighting coefficient α_p balances the contribution of V_d w.r.t to V_p . Note that V_p is independent of the observation C . Lets explain each of these two terms.

V_d is called the data potential function. It establishes the link between data and unknown, and is defined according to the application. Here, V_d is given by our TE-SGS model:

$$V_d(\mathbf{v}(\mathbf{s}), C(\mathbf{s})) = \Phi \left(\frac{\partial C(\mathbf{s})}{\partial t} + \mathbf{v}(\mathbf{s}) \cdot \nabla C(\mathbf{s}) - \left(\frac{1}{Re Sc} + D_t \right) \Delta C(\mathbf{s}) \right) \quad (20)$$

The potential function V_p corresponds to a prior term; it encodes the knowledge we have *a priori* about \mathbf{v} . In particular, it can model local dependencies between variables \mathbf{v} in a given neighbor. In equation (19), V_p acts as a regularization factor. Here, we model the spatial continuity of the velocity and express V_p as the amplitude of the velocity

vectors difference between two neighbor points (Horn and Schunk [25] and Su and Dahm [44]). Noting (u, v) the x and y components of the velocity vector \mathbf{v} , we write:

$$V_p(\mathbf{v}(\mathbf{s}), \mathbf{v}(\mathbf{t})) = \Phi(|u(\mathbf{s}) - u(\mathbf{t})|) + \Phi(|v(\mathbf{s}) - v(\mathbf{t})|) \quad (21)$$

This term will constrain the solution $\hat{\mathbf{v}}$ to be smooth spatially and uniformly.

The function $\phi(\cdot)$ is here chosen quadratic, both in the data term and regularization term. Note that our methodological framework does not prevent us from using robust functions (*e.g.* truncation function, L_1 norm) instead of a quadratic cost. This choice is motivated by its simplicity of implementation and its robustness for optimization. However, as a drawback, it tends to oversmooth the real discontinuities of the velocity field. Some authors proposed other robust functions to overcome this limitation (Black and Anandan [9] or Papenberg et al. [32]). The aim of this work is to analyse the influence of the subgrid scale transport equation model, this is the reason why we choose the quadratic simple function and we do not focus on ϕ .

Moreover, the first order derivative constraint of the velocity field (c.f. equ. (21)) can be too restrictive, depending on studied motion. However, this constraint has simple spatial coherence which allows us to properly compare TE and TE-SGS formulations. Other regularization functions more adapted to fluid motion can be incorporated, such as spatial div-curl equation (Corpetti et al. [17]), spatio-temporal equation (Weickert and Schnorr [49]) or simplified Navier Stokes equation (Ruhnau and Schnorr [35], Heitz et al. [22]).

2.3.3 Efficient pyramidal decomposition and multi-grid scheme

The acquisition time step δt is fixed during the acquisition procedure. For existing large velocity gradients on a given instantaneous image, the partial derivatives do not contain accurate motion information anymore in different zones of a same image. Generally, multi-resolution techniques is used to overcome the problem of large displacements. It has been shown that multi-resolution pyramidal decomposition, from coarser to finer resolution, is numerically useful for OF estimation in cases of large displacement (Papenberg et al. [33]).

The image resolution is progressively reduced; the set of images thus obtained form a pyramid of K different levels (Burt and Adelson [10]) (see Fig. 1). Assuming the original images are of size N^2 , then subsequent reduced images in the pyramid will generally be of size $N^2/2^{2k}$, for $k = \{1, \dots, K\}$. At each pyramidal level k , the velocity vector is $\mathbf{v}_k = \tilde{\mathbf{v}}_{k+1} + \mathbf{v}'_k$ where $\tilde{\mathbf{v}}_{k+1}$ is the (bilinearly) interpolated velocity vector computed at coarse resolution ($k+1$)

Algorithm 1: Multi-resolution/Multi-grid algorithm without warping

```

1 Pyramidal creation from level 0 (original) to K (coarsest) ;
2 Multi-Resolution Scheme ;
3 for  $k = K$  to 0 do
4   if  $k \neq K$  Consider estimated velocity at coarser level then
5      $\mathbf{v}_{k+1}^+ = \text{Interpolate}(2, \mathbf{v}_{k+1}^+)$  from  $k+1$  to  $k$  ;
6     Compute Pixel Gradients:  $\nabla C_k^+$ ,  $\Delta C_k^+$  and  $\left(\frac{\partial C^+}{\partial t}\right)_k$  ;
7   else
8     Compute Pixel Gradients:  $\nabla C_k^+$ ,  $\Delta C_k^+$  and  $\left(\frac{\partial C^+}{\partial t}\right)_k$  ;
9   Two Steps Multi-Grid ;
10  At grid level: ;
11    Compute Grid Gradients:  $\nabla C_{gk}^+$ ,  $\Delta C_{gk}^+$ ,  $\left(\frac{\partial C_{gk}^+}{\partial t}\right)_{gk}$  ;
12    Estimate  $\mathbf{v}_{gk}^{+'}$  Optimization by DDE ;
13  At pixel level: ;
14     $\mathbf{v}_k^{+'} \leftarrow \mathbf{v}_{gk}^{+'}$  Interpolation from grid to pixel level ;
15    Estimate  $\mathbf{v}_{lk}^{+'}$  Optimization by DDE ;
16     $\mathbf{v}_k^{+'} \leftarrow \mathbf{v}_{gk}^{+'} + \mathbf{v}_{lk}^{+'}$  ;
17  End Two Step Multi-Grid ;
18  Update  $\mathbf{v}_k^+ = \widehat{\mathbf{v}}_{k+1}^+ + \mathbf{v}_k^{+'}$  ;
19 Return the dense velocity field:  $\mathbf{v}_0^+$  ;
20 End Multi-Resolution ;

```

to image resolution of level k , and \mathbf{v}_k^+ is the incremental velocity at level k .

Let us first write each of our two potential functions at level k :

$$V_d(\mathbf{v}_k, C_k) = \left(\left(\frac{\partial C}{\partial t} \right)_k + \mathbf{v}_k^+ \cdot \nabla C_k - \left(\frac{1}{Re Sc} + D_t \right) \Delta C_k \right)^2 \quad (22a)$$

$$V_p(\mathbf{v}_k(\mathbf{s}), \mathbf{v}_k(\mathbf{t})) = (u_k(\mathbf{s}) - u_k(\mathbf{t}))^2 + (v_k(\mathbf{s}) - v_k(\mathbf{t}))^2 \quad (22b)$$

where

$$u_k = \tilde{u}_{k+1} + u_k' \quad v_k = \tilde{v}_{k+1} + v_k' \quad (23)$$

are respectively the x and y components of the total velocity at level k , \mathbf{v}_k .

For the sake of clarity, we do not write the dependency on \mathbf{s} in V_d (equ. 22a). The first term on the RHS, $\left(\frac{\partial C}{\partial t}\right)_k$, is approximated by $(C_1(\mathbf{s} + \delta d, t + \delta t) - C_2(\mathbf{s}, t)) / \delta t$, with $\delta d = \tilde{\mathbf{v}}_{k+1}(\mathbf{s}) \delta t$; it is the only term that depends on the velocity estimated at coarser level $\tilde{\mathbf{v}}_{k+1}$. C_1 and C_2 correspond to the two successive images at time t and $t + \delta t$, via the relation $I \propto C$. This expression differs from most existing methods, which usually rely on a wrapping step (Papenberg et al. [32], Corpetti et al. [17]). We argue here and demonstrate experimentally that warping is in fact an unnecessary

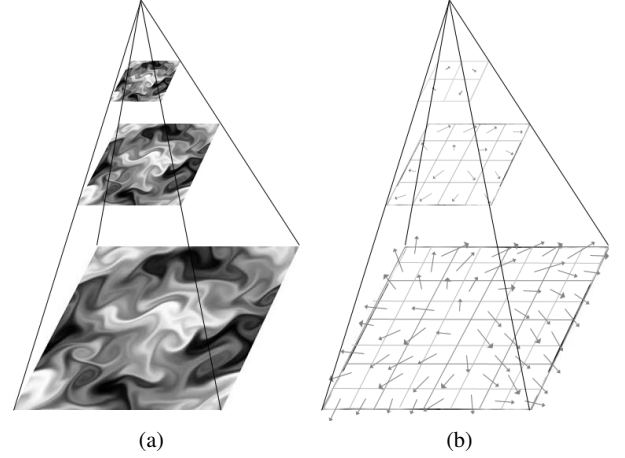


Fig. 1 Coarser to finer resolution with multiresolution representation of images (a) and corresponding estimated velocity field for each pyramidal level (b)

step which may lead to a loss of accuracy in the computation (Cassisa et al. [13]).

Therefore, at each level of the pyramid, except K , only the optimal incremental component of the velocity field is estimated. Still, in order to speed up the computation time, we further decompose $\mathbf{v}_k'(\mathbf{s})$ into a global and a local component: the global component $(\mathbf{v}_g')_k$ is defined as the average velocity increment over a cell of size pxp ; the local component $(\mathbf{v}_l')_k$ corresponds to the local deviation from $(\mathbf{v}_g')_k$ at each pixel within the cell. In practice, we first estimate $(\mathbf{v}_g')_k$, which is fast, then refine the estimation by adding a second (2D) variable $(\mathbf{v}_l')_k$ in the computation. The entire algorithm scheme is shown in Algo 1. More details can be found in Cassisa et al. [12].

2.3.4 Optimization procedure

Our total energy computed at levels $k \in \{K-1, 0\}$ of the pyramid, is fully defined by equations (19), (22a), (22b), (23), and further by the decomposition into a local component and a global component. At level $k = K$, the energy functional is given by equations (19), (20), (21). We now seek for the solution $\hat{\mathbf{v}}$ s.t.:

$$\begin{aligned} \hat{\mathbf{v}} &= \hat{\mathbf{v}}_0 = \hat{\mathbf{v}}_K + \sum_{k=K-1}^0 \hat{\mathbf{v}}_k' \\ \hat{\mathbf{v}}_k' &= \arg \min_{\mathbf{v}_k' \in \Gamma^N} E_k(\mathbf{v}_k', C_k) \\ \hat{\mathbf{v}}_K &= \arg \min_{\mathbf{v}_K \in \Gamma^N} E_K(\mathbf{v}_K, C_K) \end{aligned} \quad (24)$$

In order to minimize the energy $E_k(\cdot)$ $k \in \{K, 0\}$, we use a direct descent energy (DDE) (Snyman [41], Cassisa et al. [14]). For clarity, let's call $F(\cdot) = E_k(\cdot)$, with the appropriate change of variables. DDE will minimize $F(\mathbf{v}(\mathbf{s}), C(\mathbf{s}))$,

at each pixel \mathbf{s} , by successive iterations. At each iteration i , a small incremental random value $\delta\mathbf{v}(\mathbf{s})$ is drawn. The increment $\delta\mathbf{v}_k(\mathbf{s})$ is retained only if $F(\mathbf{v}(\mathbf{s}) + \delta\mathbf{v}(\mathbf{s}), C(\mathbf{s})) < F(\mathbf{v}(\mathbf{s}), C(\mathbf{s}))$; $\mathbf{v}(\mathbf{s})$ is then replaced by $\mathbf{v}(\mathbf{s}) + \delta\mathbf{v}(\mathbf{s})$ at point \mathbf{s} .

Because only point-wise minimization is performed, the process may converge to a local minimum of the energy: in principle, the resulting optimal solution $\hat{\mathbf{v}}$ depends on the initial value of the $\mathbf{v}(\mathbf{s}) \forall \mathbf{s}$ (chosen randomly). In order to avoid irrelevant sub-optimal local minima, we define the weighting coefficient α_p (c.f. equation 19) as a logarithm function of i , varying from 0 to α_p^{max} . This way, the solution is mainly driven by the data term at the beginning of the iterations, while at the end of the iterations the quadratic prior term takes more importance. It is worth noticing that similar approach has been used successfully by others before (Baillole et al. [4]). Coupled to the multi-resolution technique, we observe experimentally that the solution at convergence is stable.

3 Description of validation tests

3.1 Numerical Simulation (DNS) of a scalar mixing in a turbulent flow

Data acquisition

A passive scalar concentration synthetic image sequence is generated by Direct Numerical Simulation (DNS) for a 2D turbulence of an incompressible fluid. The 2D vorticity equations and the equation of advection-diffusion are used to calculate the velocity and passive scalar concentration fields at each instant. The size of each frame is 256×256 pixels. We have a sequence of 100 successive frames. The Reynolds number is $Re = 3000$ and the Schmidt number is $Sc = 0.7$. This sequence was provided by the Cemagref of Rennes. Details can be found in Carlier and Heitz [11].

Validation

Using the true velocity field from the DNS computation, we calculated the statistical errors to evaluate quantitatively the quality of algorithm results. In a standard way (Barron et al. [6], Baker et al. [5]), we computed the Average Angle Error (AAE) and RMS Velocity Error as follows:

$$AAE = \frac{1}{S} \sum_{s=0}^S \arccos \left(\frac{\mathbf{v}_c^+(s) \cdot \mathbf{v}_e^+(s)}{\|\mathbf{v}_c^+(s)\| \|\mathbf{v}_e^+(s)\|} \right) \quad (25a)$$

$$RMS = \frac{1}{S} \sqrt{\sum_{s=0}^S \|\mathbf{v}_c^+(s) - \mathbf{v}_e^+(s)\|^2} \quad (25b)$$

with \mathbf{v}_c^+ and \mathbf{v}_e^+ are respectively the DNS and the estimated velocity vector fields.

We also compare our results with the state-of-the-art on fluid motion analysis introduced in Corpetti et al. [17]. Note that, for passive scalar concentration spreading sequence, cross-correlation algorithms, as the one of PIV Davis Lavision software, are not adapted because no particle was included in the simulation; it is thus not appropriate for comparison with our approach.

The model proposed in Corpetti et al. [17] uses a flow equation based on 2D projection of continuity equation (ICE). The authors defines a regularization term based on divergence and vorticity (DivCurl) constraints of the flow, which is specifically adapted to velocity field of fluids. We note it the ICE-DivCurl model. Parameter setting for ICE-DivCurl were not available. Only the estimated velocity field were provided by the authors. These estimated velocity fields are published in [31] applying on the same scalar DNS sequence as presently.

For incompressible fluid with apparent molecular diffusion or high Reynolds number, ICE-DivCurl and TE methods become similar to the differential optical flow (see sec.1). They only differ from the regularization function. For low Reynolds number, turbulent diffusion is small compare to convective terms, TE-SGS is similar to TE. However, when Re becomes high, turbulent diffusion cannot be anymore neglected. This is especially important in this case (this is for the majority of satellite images for instance) as the spatial resolution is far to reach the smallest turbulent scales. The coefficient D_t models the small scale effects in TE-SGS equation.

Our algorithm settings

We set identically the parameters for TE and TE-SGS for a fair comparison. Maximum displacement field between two successive images is about $\mathbf{v}_{max} = -\mathbf{v}_{min} = 3.5$ pixels. We use a 3-level pyramidal decomposition and a grid size of 2×2 pixels for multigrid. Images are first filtered by a Gaussian filter of variance $\sigma^2 = 1$ at each level of the pyramid. This reduces the influence of noise. Applying Gaussian filter suppresses small scales of the DNS. Moreover, the processed DNS image sequence only contain 1 over 10 time DNS calculation. The weighting coefficient α_p^{max} is set to 1. For TE-SGS, the coefficient D_t was determined using the equation 15 and the power spectrum of the case with $K_c = 33$ and $C_{sgm} = 0.1$. This gives us $D_t \approx 0.25$.

3.2 Wind tunnel experiment

Data acquisition

Experiment and image acquisition were conducted at LMFA (Simoens et al. [38, 39]), in order to study the dispersion of

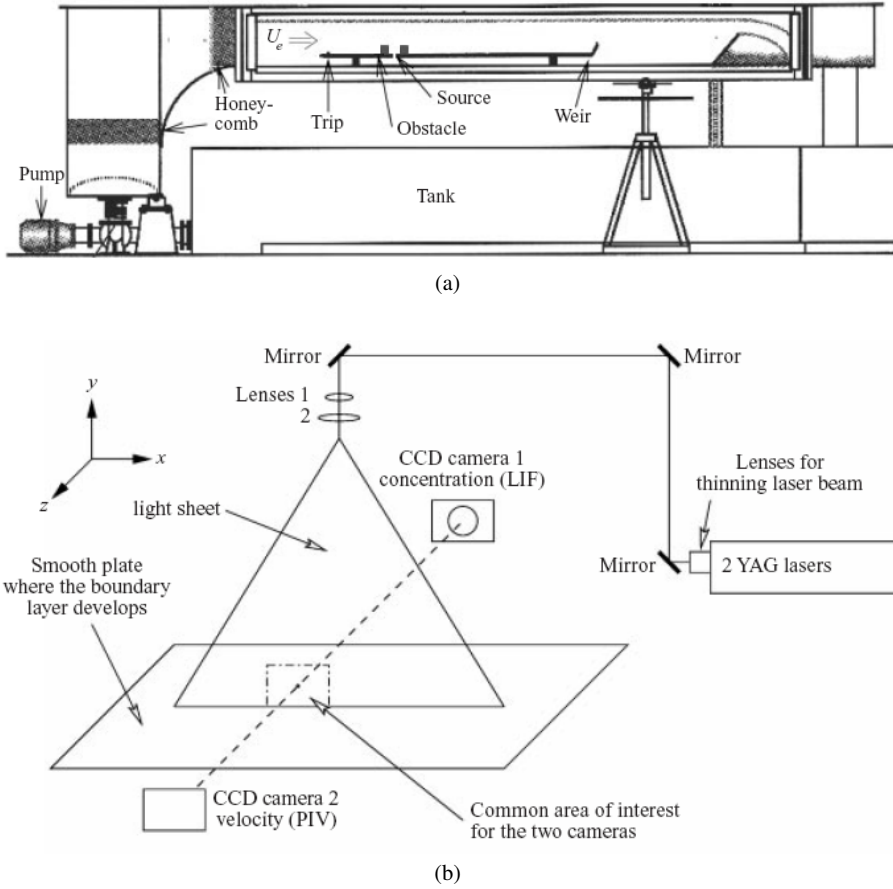


Fig. 2 Sketch of channel (a) and optical set-up arrangements to create laser light sheet (b).

passive scalar within an atmospheric boundary layer in presence of obstacles. The source is located in the middle of a canyon represented by two lines of squares whose sections are h^2 . Obstacles are transversally disposed in order to be perpendicular to the mean flow; the distance between them is $h = 1\text{cm}$. The momentum Reynolds number at source location without obstacle is $Re \approx 10^3$ and the Schmidt number is $Sc \approx 10^6$. The sketch of the tunnel is represented in Figure 2a. The passive scalar is incense smoke. At a given zoom, this provides images of the solid sub-microscopic particles constituting smoke. There, like at zoom of Mie scattering diffusion, light is linked to the number of solid particles leading to their concentration. We used the images obtained with the higher zoom that individualizes particles.

The acquisition was made by synchronization of two YAG lasers and a CCD camera. YAG lasers delivered 300mJ energy per pulse and had a pulse frequency of 10Hz that determined the acquisition frequency of image pairs. Time step between the two laser pulses, δt , for first and second image acquisition of each pair, was 0.2ms . Synchronization between camera and laser pulses was achieved by Lavisson device. PIV from software Davis Lavisson allowed to obtain

good results using a recursive mesh size method with refinement from 128×128 to 4×4 pixels. The optical set-up arrangements are shown in Figure 2b. More details can be found in Vincont et al. [48].

Validation

We compare our results with PIV technique from Davis LaV-ision software [28] on mean velocity field profiles and RMS fluctuated velocity field profiles.

Our algorithm settings

As for DNS sequence, settings are the same for TE and TE-SGS. Maximum displacement of the velocity field between two instants t and $t + \delta t$ is about 6 pixels. We use a 3-level pyramidal decomposition and a grid size of 2×2 pixels for multigrid resolution. The images are filtered by a Gaussian filter of variance $\sigma^2 = 1$. α_p^{max} equals to 1. For TE-SGS, the coefficient D_t was determined using the equation 15. The power spectrum was the one by Spalart [42] cited in [48] as characterizing the boundary layer of their experiment.

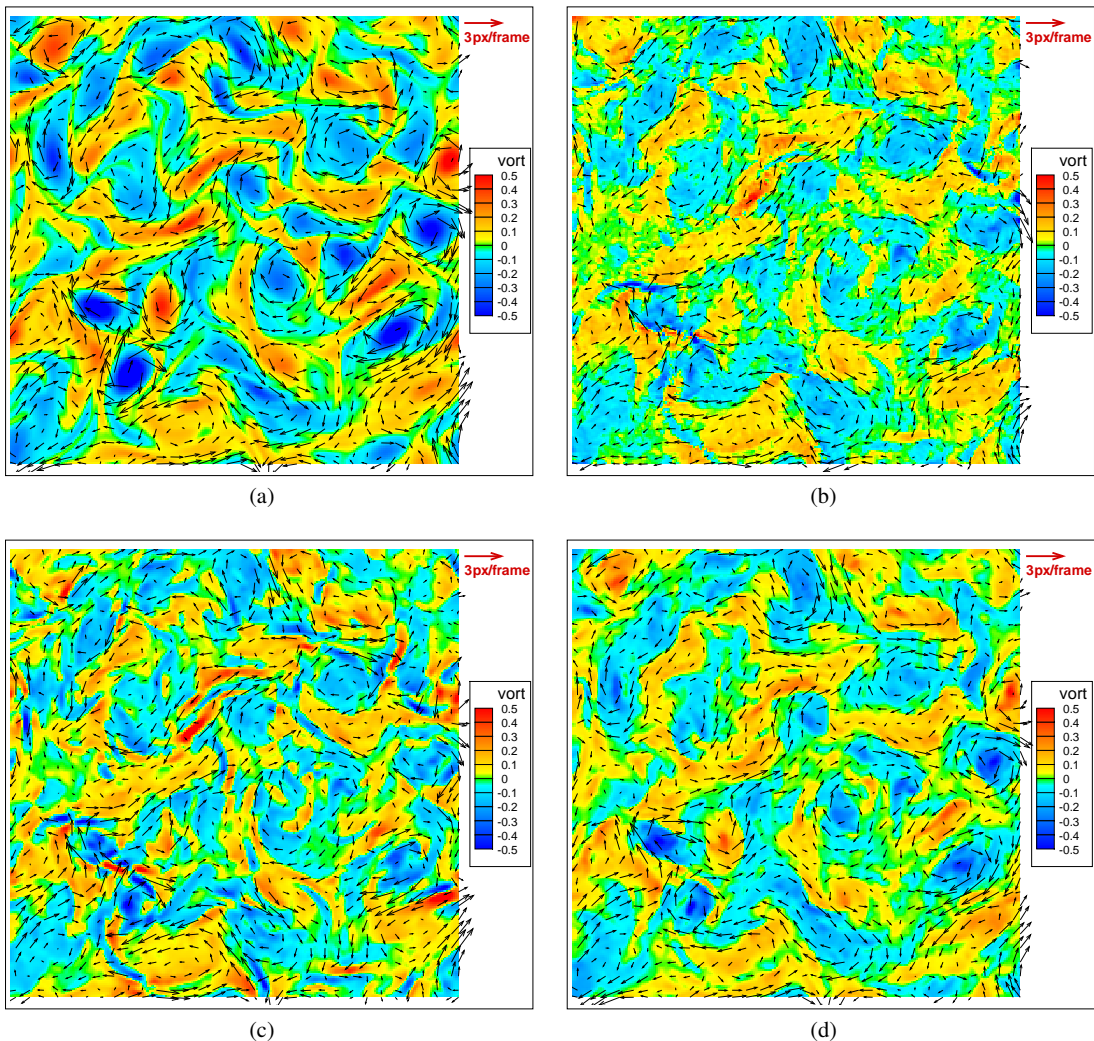


Fig. 3 Instantaneous results on DNS sequence at times ($t = 50$): exact DNS vorticity map (a), estimated vorticity maps with superposition of flow vectors obtained by ICE-DivCurl (b), TE (c) and TE-SGS (d). Input passive scalar concentration field at time $t = 50$ is illustrated in figure 4(a).

The filter size is deduced from the given spatial resolution, $K_c = 211.5$ and $C_{sgm} = 0.1$. This gives us $D_t \approx 2$.

4 Results and discussion

4.1 Validation of the subgrid scale model on synthetic DNS image sequences

Figure 3 shows the estimated velocity field and vorticity map obtained from each method at time $t = 50$. Figure 3(a) shows the exact DNS vorticity fields (with velocity vector superposed to the vorticity map). Figure 3(b) illustrates the estimated fields from ICE-DivCurl; (c) and (d) are respectively the estimated fields from our TE and TE-SGS algorithms. The color legend is identical for all these results. The vector field and vorticity map obtained from ICE-DivCurl and

the ones obtained from TE are visually very similar. Lets remind that the ICE-DivCurl and TE differ only by the regularization term and the molecular diffusion factor; however, in this DNS simulation with high Reynolds number ($Re = 3000$), the molecular diffusion term of equation (12) will be negligible ; therefore only the regularization (which in ICE-DivCurl was specifically designed for fluid motion) distinguishes the two models. TE-SGS performs better than TE and ICE-DivCurl: TE-SGS detects more accurately the vortices and globally behaves more like the original DNS fields.

Figure 4 illustrates an example on a zoom area of a passive scalar concentration field image at time $t = 50$ where vortices are strong. Figures 4(a) and 4(b) show the extracted and zoomed passive scalar concentration field area. In Figures 4(d), (e), (f), are represented, respectively, the divergence and vorticity maps and the DNS exact vector field.

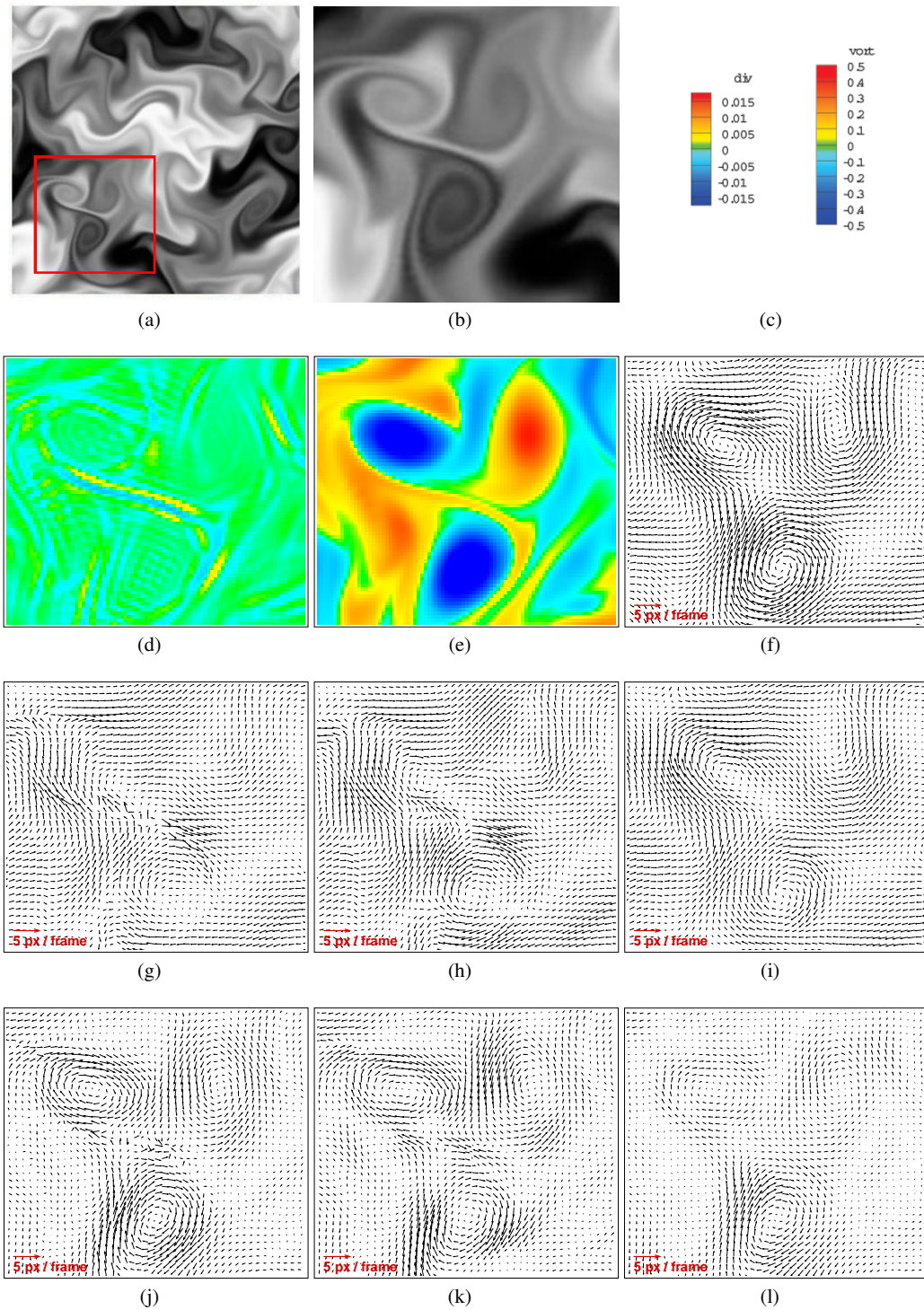


Fig. 4 Illustration over a zoomed area at time $t = 50$. Area representation on passive scalar concentration field image (a,b). Exact DNS divergence (d) and vorticity (e) maps (color map legend (c)) and exact DNS flow vector field (f). Estimated velocity vector field for ICE-DivCurl (g), TE (h) and TE-SGS (i) methods. (j,k,l) represent the velocity difference between exact DNS and estimated velocity for ICE-DivCurl, TE and TE-SGS methods respectively.

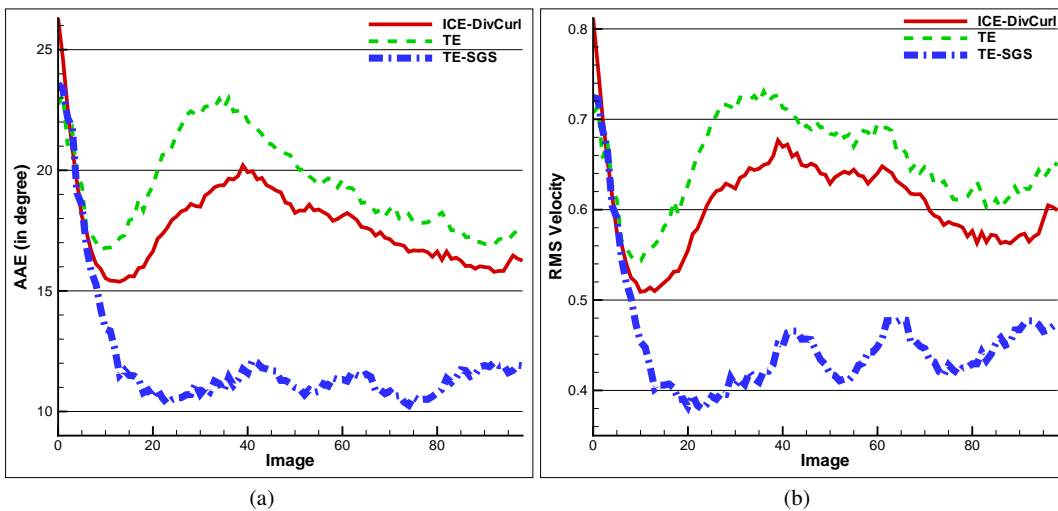


Fig. 5 AAE (a) and RMS (b) errors of ICE-DivCurl, TE and TE-SGS for DNS passive scalar concentration sequence.

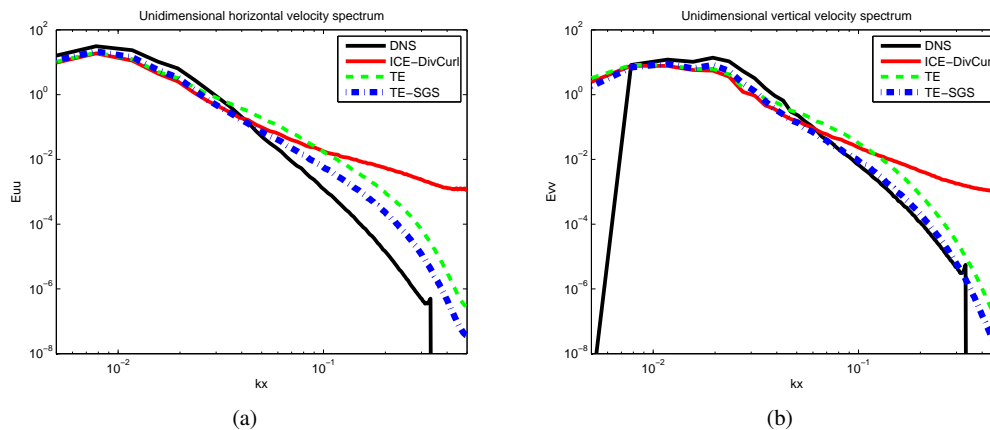


Fig. 6 Power spectral analysis of the turbulent horizontal (a) and vertical (b) velocity components over the lines (log-log scale). Exact DNS spectrum (black) is compared with spectra obtained with ICE-DivCurl (red) TE (green) and TE-SGS (blue) methods.

The third row in Figures 4(g), (h), and (i) show the estimated velocity vector fields computed from ICE-DivCurl, TE and TE-SGS methods. For a better comparison, we represent the difference velocity vector fields between the exact DNS and the estimations in Figures 4(j), (k) and (l) from ICE-DivCurl, TE and TE-SGS methods respectively. On this figures, we can see that estimated velocity field from TE-SGS is closer to the DNS results than the other methods. TE and ICE-DivCurl show similar difficulties in retrieving vortices around area of strong concentration variations. The subgrid model in TE-SGS seems to overpass these difficulties.

Figure 5 shows the statistical error AAE (left) and RMS (right) for the 100 successive images. The evolution of TE error has the same behaviour as ICE-DivCurl for both AAE

and RMS. This confirms the remarks made above. The TE estimation is however slightly less accurate. It is quite normal, because we use a first order quadratic regularization function while ICE-DivCurl uses a robust semi-quadratic function of div-curl regularization that is more appropriate to fluid motion. TE-SGS model, including subgrid scale model in passive scalar transport equation, provides a strong improvement in the estimation of the velocity field compared to TE. Estimations are also much better than ICE-DivCurl. The evolution error, over the sequence, behaves differently than TE and ICE-DivCurl methods. The TE-SGS method deals with limitations due to the lack of information on passive scalar images and retrieves a closer velocity field compare to the exact passive scalar motion.

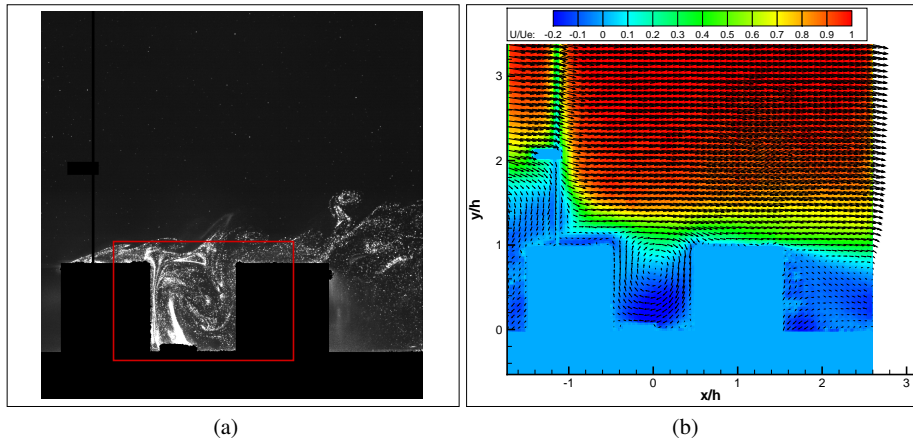


Fig. 7 Instantaneous Mie scattering diffusion image from solid particle seeding the flow with 2 obstacles (a) and amplitude map of the average horizontal velocity with the velocity vector representation obtained by PIV (b)

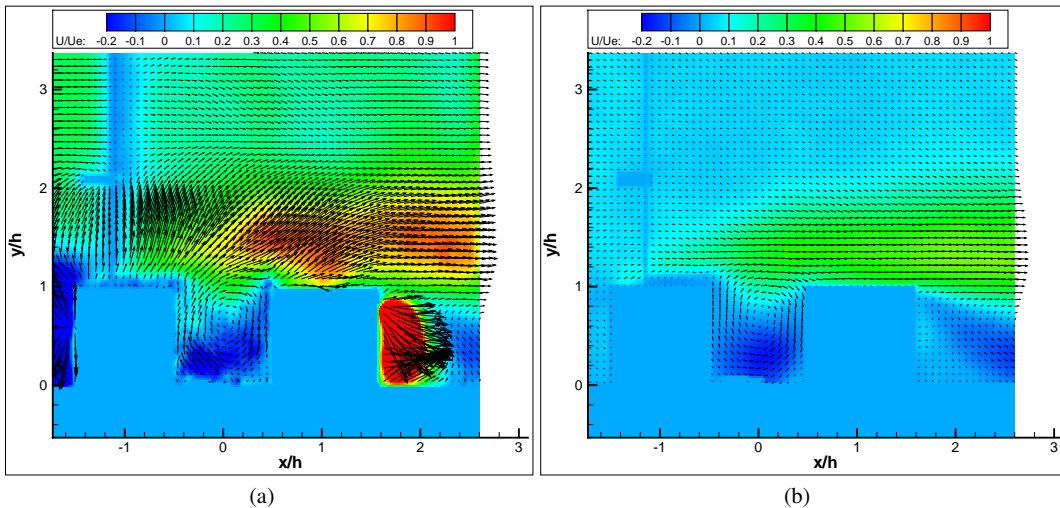
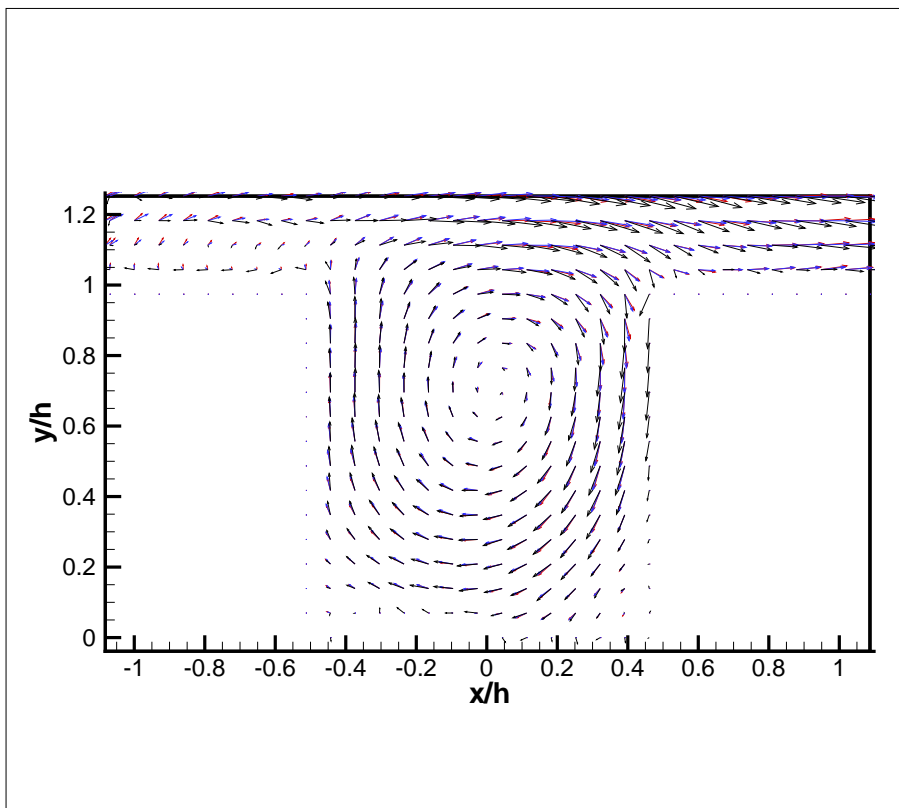


Fig. 8 Maps of amplitude of horizontal velocity with mean vector representation of velocity fields obtained by the method of to the original sequence (a) and pretreated (b)

The Figure 6(a) and 6(b) show plots of the average kinetic energy spectra of horizontal (left) and vertical (right) velocity components. We can see that the spectrum obtained by TE-SGS (blue) method is closer to the exact DNS spectrum (black) than the ones obtained by TE (green) and ICE-DivCurl (red) methods. Observed differences between TE and ICE-DivCurl results traduce the fact that TE velocity field is smoother than the one from ICE-DivCurl. It is due to the regularization function and the importance of the weighting coefficient. As, we set the same parameters for TE and TE-SGS methods, we cannot only explain the differences between the spectrum by a less noisy field. We observe, for both large and small wavelengths that TE-SGS method gives a better representation of the velocity spectrum. The pro-

posed subgrid formulation improves the shape of the flow field while performing a better estimation of the finest structures.

One important conclusion to draw from these experiments, is that, improving the data term of the energy functional—in particular via a ‘physical’ modeling such as our TE-SGS—is a necessary step to estimate a velocity field closer to the exact ground truth. The role of the regularization term, thought important, is not as crucial as the role of the data term. This can be understood by observing that the main “driving force” which leads the algorithm towards the optimal solution is precisely the data energy, while the regularisation is acting “only” to smooth out unacceptable solutions.



(a)

Fig. 9 Mean velocity field for the study area with 200 pairs of images with PIV (a) (black arrows in (d)), our method TE (b) (blue arrows in (d)) and TE-SGS (c) (red arrows in (d)). In (d) superimposed estimated fields. The color map represents the displacement amplitude normalized.

4.2 wind tunnel PIV acquisition sequence

In this subsection evaluate the robustness of our approach on solid particles seeding a flow. For this experiment, we have a series of 200 pairs of images for PIV analysis. We compute instantaneous velocity fields and average these fields. Figure 7 shows an instantaneous image of the scattering diffusion intensity from solid particle seeding the flow (Fig. 7(a)) and the mean velocity field, over the 200 pairs, from PIV results (Fig. 7(b)). On background of the PIV mean velocity field, we visualize the horizontal velocity component amplitude color map. Length and velocity scales are normalized by length h and outside boundary layer velocity $U_e \approx 2.3m.s^{-1}$.

On input images, we define a binary mask that identifies the ground and obstacles. Notice that we have a vertical line in the mask at the front of the first obstacle. It is due to a burnt pixel column of the camera. This line influences the estimation of the velocity field around this area as we can see on Figure 7(b). However, this line is far from the canyon where the test is significant. The mask is used to help the algorithms not to be disturbed by light reflection on the ana-

lyzed area (on the obstacle walls and flat plane of the tunnel). PIV Davis software can take into account this mask. In our TE-SGS algorithm, we add the possibility to use a mask. Velocity value in the mask area is set to 0. Graph edges between a pixel on the border and a pixel in the mask is deleted. Estimation of the velocity field at the mask border is then not influenced by inside border information.

These laboratory experiment results are very sensitive to the quality of acquisitions. Measured image intensity depends on the light exposure on CCD captors. The intensity contains information on seeding particle concentration but also information from experiment materials and noise. As mentioned in section 2.1, we consider in this work that image intensity is directly linked to solid particle concentration. In practice, this is not the case as main part of particle images are individualized. We had then to identify and suppress experimental noise to be able to correctly apply TE-SGS.

This noise is due to two main causes:

1. The reflections of light on the walls. This results in a background image. It is obtained in the same experimental conditions without seeding the flow.

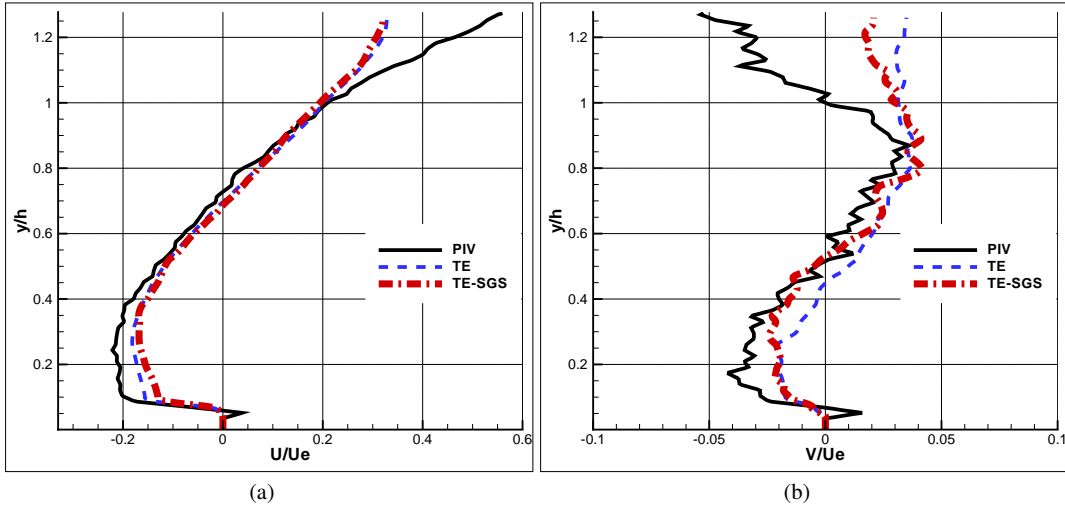


Fig. 10 Vertical profiles of average velocity field of normalized a) horizontal and b) vertical components with PIV, TE and TE-SGS methods. The profile is taken at the center of the canyon ($h = 0$)

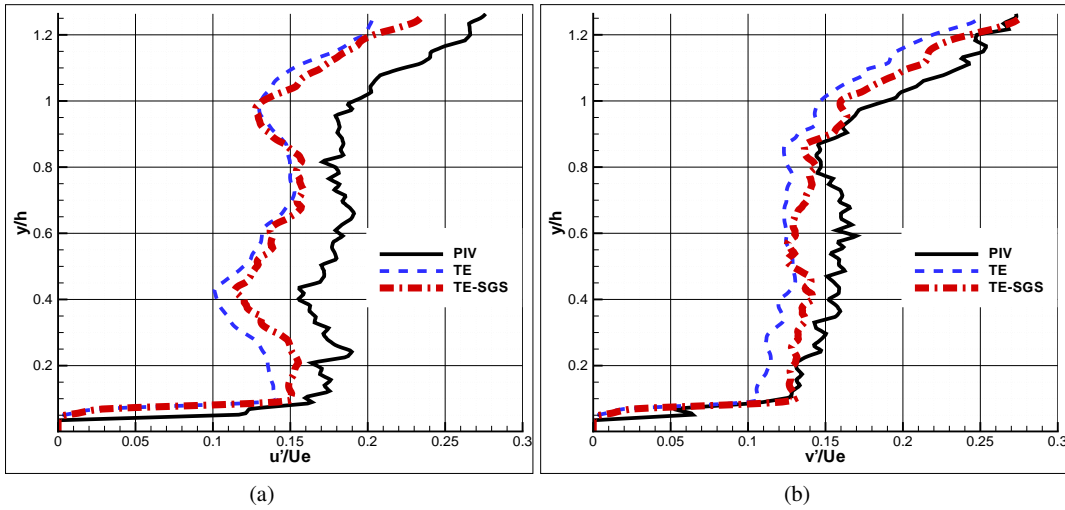


Fig. 11 Vertical profiles of the RMS fluctuating field of normalized a) horizontal and b) vertical components with PIV, TE and TE-SGS methods. The profile is taken at the center of the canyon ($h = 0$)

- The laser pulse frequency of a laser that is too low to generate pulse for both images. Thus, images 1 and 2 of a pair came from two pulses of two different lasers. Laser light intensity is then different for both images. This results on an independent brightness variation between images 1 and 2 in a pair. Such noise was classically removed as in Ayrault and Simoens [3].

We preprocessed the image pairs to remove the noise and to represent dimensionless information of the particle intensity image.

Figure 8 shows the computed mean velocity field obtained by the TE algorithm on the original images (left) and on the preprocessed images (right). Without preprocessing,

estimated field is strongly perturbed around particle intensity contours. Particle intensity contours are the most affected area by light variations due to experimental noise; preprocessing proves to remove this light variations. The estimated field on preprocessed images is not influenced by experimental noise. It is more relevant than estimated velocity field on original sequence and it is coherent with PIV field (Fig. 7(b)). We can also observe that TE algorithm does not estimate correctly the velocity field over the entire experimental domain. Our approach computes the velocity field of the fluid based on scalar transport equation. Motion field can only be computed where there is enough particle seeding the field. For $y/h \geq 1.3$, there is no more solid particle

concentration. Due to a background fluid particle seeding in the tunnel, PIV can retrieve the flow field.

To compare PIV, TE and TE-SGS, we focus the analysis on particle concentration displacement inside and close around the canyon. Figure 9 shows the mean velocity field vectors from PIV, TE and TE-SGS methods. Results for all methods are similar. To exhibit clearly difference between TE and TE-SGS approaches, we plot the vertical profiles of normalized horizontal (left) and vertical (right) velocity components at the middle of the canyon. Figure 10 represents the profiles for the mean velocity field and Figure 11 shows the RMS profiles for the different methods. On these figures, it seems that TE-SGS method estimates a better RMS and mean velocity field. It tends to retrieve a profile closer to PIV than TE does.

Note that the experiments was done on PIV Mie scattering diffusion requirements with particle density adapted to Mie diffusion approach. For further concentration field determination, particle concentration is thus not fully distributed over the image domain. This can introduce locally no results.

However, our TE model can correctly estimates the flow field over scalar concentration requirement area. TE-SGS method allows to improve flow field estimation and characteristic of the flow.

5 Conclusion

The subgrid transport equation we have proposed in this paper takes into account the limitations of observed information in images, incorporating a sub-pixel scale model based on a turbulent diffusion in the scalar transport equation. Validation on synthetic and experimental sequences, shows that the new model improves the estimation of the velocity field for study of passive scalar concentration propagation and is robust enough to be applied to non homogeneous solid particle seeding displacements. Subgrid scale model advantages are less important on experimental acquisitions because the illustrated experiment does not fully represent the passive scalar concentration field (in the original laboratory experiment concentration field is obtained only for one instant as this was sufficient for obtaining mass fluxes). However, on the DNS sequence, subgrid scale model outperforms existing optical flow algorithms by considering influence of small scales at subgrid level on the filtered flow field. TE-SGS better estimates vortices by modelling the turbulence influence. It would be interesting to combine advantages of PIV methods with optical flow (Heitz et al. [22]) not only by constraining the optical flow estimation by the correlation estimations, but also by using a confident weighting coefficient depending on the properties of the studied flow (solid particle or passive scalar transport). A more complex definition

of the turbulent diffusion could also bring an improvement to our model (Smagorinsky [40], Cui et al. [18]).

Acknowledgements The authors wish to thank the team of the European project Fluid in Rennes. Especially, Johan Carlier for giving us the DNS scalar synthetic sequence and Thomas Corpetti for providing us the estimated fields of his OF algorithm for this DNS sequence. This work is partially supported by the 863 program of the Chinese Ministry of Science and Technology and by Tandem - Erasmus Mundus Program.

References

1. Adrian, R.J.: Particle-Imaging Techniques for Experimental Fluid Mechanics. *Annual Review of Fluid Mechanics*, **23**, pp. 261–304, (1991).
2. Amini, A.A. : A scalar function formulation for optical flow: applications to X-ray imaging. In: *Workshop on Biomedical Image Analysis*, pp. 117–123 (1994)
3. Ayrault, M., Simoens, S.: Turbulent concentration determination in gas flow using multiple ccd cameras. *Journal of Flow Visualization and Image Processing*, **2**(2), pp. 195–208 (1995)
4. Bailloeuil, T., Prinnet, V., Serra, B., Marthon, P.: Spatio-temporal prior shape constraint for level set segmentation. In: *Energy Minimization Methods in Computer Vision and Pattern Recognition (EMMCVPR)*, LNCS 3757 Springer-Verlag, pp.503–519 (2005)
5. Baker, S., Roth, S., Scharstein, D., Black, M.J., Lewis, J.P., Szeliski, R.: A Database and Evaluation Methodology for Optical Flow. In: *International Conference on Computer Vision (ICCV)*, pp. 1–8 (2007)
6. Barron, J.L., Fleet, D.J., and Beauchemin, S.: Performance of optical flow techniques. *International Journal of Computer Vision*, **12**(1), pp. 43–77 (1994)
7. Batchelor, G. K.: *An introduction to fluid dynamics*. Cambridge University Press (1967)
8. Bereziat, D., Herlin, I., Younes, L.: Motion estimation using a volume conservation hypothesis. In: *International Conference on Acoustic, Speech and Signal Processing (ICASSP)*, pp. 3385–3388 (1999). Phoenix
9. Black, M., Anandan, P.: The robust estimation of multiple motions: Parametric and piecewise-smooth flow-fields. *Computer Vision and Image Understanding*, **63**(1), pp. 75–104 (1996)
10. Burt, P., Adelson, E.: The Laplacian pyramid as a compact image code. *Transactions on Communications*, **31**(4), pp. 532–540 (1983)
11. Carlier, J., Wieneke, B.: Report on production and diffusion of fluid mechanics images and data. Technical Report, Fluid Project deliverable 1.2 (2005)
12. Cassisa, C., Prinnet, V., Shao, L., Simoens, S., Liu, C.: Optical flow robust estimation in a hybrid multi-resolution MRF framework. In: *International Conference on Acoustics, Speech and Signal Processing (ICASSP)*, pp. 793–796 (2008)
13. Cassisa, C., Simoens, S., Prinnet, V.: Two-frame optical flow formulation in an unwrapping multi-resolution scheme. In: *14th Iberoamerican Conference on Pattern Recognition (CIARP)*, LNCS 5856 Springer-Verlag, pp. 790–797 (2009)
14. Cassisa, C., Simoens, S., Prinnet, V.: Local Vs Global Energy Minimization Methods: Application to Stereo Matching. In: *International Conference on Progress in Informatics and Computing (PIC)* (2010)
15. Chollet, J.P., Lesieur, M.: Parameterisation for small scales of three dimensional isotropic turbulence using spectral closure. *Journal of the Atmospheric Sciences*, **38**, pp. 2747–2757 (1981)

16. Comte-Bellot, G., Corrsin, S.: The use of a contraction to improve the isotropy of grid generated turbulence. *Journal of Fluid Mechanics*, **25**, pp. 657-682 (1966)
17. Corpetti, T., Heitz, D., Arroyo, G., Menin, E., Santa-Cruz, A.: Fluid experimental flow estimation based on an optical-flow scheme. *Experiments in Fluids*, **40**(1), pp. 80-97 (2006)
18. Cui, G., Xu, C., Fang, L., Shao, L., Zhang, Z.: A new subgrid eddy-viscosity model for large-eddy simulation of anisotropic turbulence. *Journal of Fluid Mechanics*, **582**, pp. 377-397 (2007)
19. Deradorff, J.W. : A numerical study of three-dimensional turbulent channel flow at large Reynolds numbers. *Journal of Fluid Mechanics*, **41**, pp. 453-480 (1970)
20. Garbe, C.S., Spies, H., Jähne, B. : Estimation of surface flow and net heat flux from infrared image sequences. *Journal of Mathematical Imaging and Vision*, **19**, pp. 159-174 (2003)
21. Haussecker, H.W., Fleet, D.J. : Computing optical flow with physical models of brightness variation. In: *Conference on Computer Vision and Pattern Recognition*, **2**, pp. 760-767 (2000)
22. Heitz, D., Heas, P., Memin, E., Carlier, J.: Dynamic consistent correlation-variational approach for robust optical flow estimation. *Experiments in Fluids*, **45**(4), pp. 595-608 (2008)
23. Heitz, D., Memin, E., Schnorr, C.: Variational fluid flow measurements from image sequences : synopsis and perspectives. *Experiments in Fluids*, **48**(3), pp. 369-393 (2010)
24. Heas, P., Memin, E., Papadakis, N., Szantai, A.: Layered Estimation of Atmospheric Mesoscale Dynamics From Satellite Imagery. *Geoscience and Remote Sensing, IEEE Transactions*, **45**(12), pp. 4087-4104 (2007).
25. Horn, B., Schunck, B.: Determining optical flow. *Artificial Intelligence*, **17**(1-3), pp. 185-203 (1981)
26. Kolmogorov, A.N. : The local structure of turbulence in incompressible viscous fluid for very large Reynolds numbers. *USSR Academy of Sciences*, **30**, pp. 299-303 (1941)
27. Kolmogorov, V., Zabih R.: What Energy Functions can be Minimized via Graph Cuts? In *IEEE Transactions on Pattern Analysis and Machine Intelligence (PAMI)*, **26**(2):147-159, February 2004.
28. LaVision-DaVis: Software for Intelligent Imaging (2005)
29. Liu, T., Shen, L.: Fluid flow and optical flow. *Journal of Fluid Mechanics*, **614**, pp. 253-291 (2008)
30. Nomura, A., Miike, H., Yokoyama, E.: Detecting motion and diffusion from a dynamic image sequence. *Transactions of IEEE Japan (in Japanese)*, **115**(C), pp. 403-409 (1995)
31. Papadakis, N. and Mémin, E.: Variational assimilation of fluid motion from image sequences. *SIAM Journal on Imaging Science*, **4**, pp. 343-363 (2008)
32. Papenberg, N., Bruhn, A., Brox, T., Didas, S., Weickert, J.: Highly accurate optic flow computation with theoretically justified warping. *International Journal of Computer Vision*, **67**(2), pp. 141-158 (2006)
33. Papenberg, N., Bruhn, A., Brox, T., Weickert, J.: Numerical justification for multi-resolution optical flow computation. In: *International Workshop on Computer Vision and Image Analysis (IWCVIA)*, **26**, pp. 7-12 (2003)
34. Ribault, C., Sakar, S., Stanley, S.: Large eddy simulation of evolution of a passive scalar in plane jet. *American Institute of Aeronautics and Astronautics Journal*, **39**, pp. 1509-1516 (2001)
35. Ruhnau, P., Schnorr, C.: Optical stokes flow estimation : an imaging-based control approach. *Experiments in Fluids*, **42**(1), pp. 61-78 (2007)
36. Shao, L., Bertoglio, J.P., Michard, M.: Large Eddy Simulation of the Interaction between Two Distinct Turbulent Velocity Scales. in *Advances in Turbulence 3*, Ed. Springer-Verlag, pp. 101-112. (1990)
37. Shao, L., Michard, M., Bertoglio, J.P.: Effect of a Solid Body Rotation on the Turbulent Transport. *Turbulent Shear Flow 8*, Selected paper, Ed. Springer-Verlag, pp. 369-381 (1991).
38. Simoens, S., Ayrault, M., Wallace, J.: The flow across a street canyon of variable width - part 1: Kinematic description. *Atmospheric Environment*, **41**, pp. 9002-9017 (2007)
39. Simoens, S., Wallace, J.: The flow across a street canyon of variable width - part 2: Scalar dispersion from a street level line source. *Atmospheric Environment*, **42**, pp. 2489-2503 (2008)
40. Smagorinsky, J.: General circulation experiments with the primitive equations i. the basic experiment. *Monthly Weather Review*, **91**, pp. 99-164 (1963)
41. Snyman, J.A. : *Practical Mathematical Optimization: An introduction to basic optimization theory and classical and new gradient-based algorithms*. Kluwer Academic Publishers, Dordrecht, The Netherlands (2004)
42. Spalart, P.: Direct simulation of a turbulent boundary layer up to $Re_\theta = 1410$. *Journal of Fluid Mechanics*, **187**, pp. 61-98 (1988)
43. Stan, Z.L. : *Markov Random Field Modelling in Image Analysis*, 2nd ed. Springer-Verlag (2001)
44. Su, L. and Dahm, W.: Scalar imaging velocimetry measurements of the velocity gradient tensor field in turbulent flows. i. assessment of errors. *Physics of Fluids*, **8**, pp. 1869-1882 (1996)
45. Su, L. and Dahm, W.: Scalar imaging velocimetry measurements of the velocity gradient tensor field in turbulent flows. ii. experimental results. *Physics of Fluids*, **8**, pp. 1883-1906 (1996)
46. Suter, D.: Motion estimation and vector splines. In: *International Conference on Computer Vision and Pattern Recognition (CVPR)*, pp. 939-942 (1994).
47. Szeliski R., Zabih R., Scharstein D., Veskler O., Kolmogorov V., Agarwala A., Tappen M. and Rother C., A Comparative Study of Energy Minimization Methods for Markov Random Fields with Smoothness-Based Priors, In *IEEE Transactions on Pattern Analysis and Machine Intelligence (PAMI)*, **30**(6):1068-1080, June 2008.
48. Vincont, J., Simoens, S., Ayrault, M., Wallace, J.: Passive scalar dispersion in a turbulent boundary layer from a line source at the wall and downstream of an obstacle. *Journal of Fluid Mechanics*, **424**, pp. 127-167 (2000)
49. Weickert, J., Schnorr, C.: Variational optic flow computation with a spatio-temporal smoothness constraint. *Journal of Mathematical Imaging and Vision*, **14**(3), pp. 245-255 (2001)
50. Winkler, G. : *Image Analysis, Random Fields, and Dynamic Monte Carlo Methods: A Mathematical Introduction*. Springer (1995)
51. Zhou, L., Kambhamettu, C., Goldgof, D.B.: Fluid structure and motion analysis from multi-spectrum 2d cloud image sequences. In: *International Conference on Computer Vision and Pattern Recognition (CVPR)*, **2**, pp. 744-751 (2000)